Image-Guided Robotic Flexible Needle Steering

Daniel Glozman and Moshe Shoham, *Associate Member, IEEE*

***Abstract*—This paper presents a robotic system for steering under real-time fluoroscopic guidance a flexible needle in soft tissue. Given a target and possible obstacle locations, the computer calculates the flexible needle-tip trajectory that avoids the obstacle and hits the target. Using an inverse kinematics algorithm, the needle base maneuvers required for a tip to follow this trajectory are calculated, enabling a robot to perform controlled needle insertion. Assuming small displacements, the flexible needle is modeled as a linear beam supported by virtual springs, where the stiffness coefficients of the springs can vary along the needle. Using this simplified model, the forward and inverse kinematics of the needle are solved analytically, enabling both path planning and path correction in real time. The needle shape is detected in real time from fluoroscopic images, and the controller commands the needle base motion that minimizes the needle tip error. This approach was verified experimentally using a robot to maneuver the base of a flexible needle inserted into a muscle tissue. Along the 40-mm trajectory that avoids the obstacle and hits the target, the error stayed below the 0.5-mm level. This study demonstrates the ability to perform closed-loop control and steering of a flexible needle by maneuvering the needle base so that its tip achieves a planned trajectory.**

***Index Terms*—Biomedical imaging, flexible structures, medical treatment, robots.**

I. Introduction

THE trend of contemporary medicine is towards less invasive and more localized therapy. Many routine treatments employed in modern clinical practice involve percutaneous insertion of needles and catheters for biopsy and drug delivery. The aim of a needle insertion procedure is to place the tip of an appropriate needle safely and accurately in a lesion, organ, or vessel. Examples of treatments requiring needle insertions include vaccinations, blood/fluid sampling, regional anesthesia, tissue biopsy, catheter insertion, cryogenic ablation, electrolytic ablation, brachytherapy, neurosurgery, deep brain stimulation, and various minimally invasive surgeries.

In general, complications of percutaneous needle insertion are due to poor technique and needle placement [1]. Physicians and surgeons often rely only upon kinesthetic feedback from the tool that they correlate with their own mental 3-D perception of anatomic structures. However, this method has significant limitations since, as the needle penetrates the tissue, the tissue deforms and, thus, even when working with straight rigid needles, the needle might miss the target [2]. To improve needle placement, rigid needles can be maneuvered under image guidance. Furthermore, Alteroviz *et al.* [3] have proposed a way to predict rigid-needle placement error in prostate brachytherapy procedures and to correct for this error by choosing an alternative insertion point. Despite such advances in rigid-needle placement, in some cases it remains a problem that rigid needles lead to excessive, injurious pressure on tissues.

An alternative approach to ensuring the success of percutaneous procedures is to employ thin and flexible needles. There are numerous advantages to using such needles. According to retrospective studies that examined the relationship between postbiopsy behavior and biopsy needle diameter, less serious complications occur with fine (less than 1 mm) biopsy needles than with standard coarse needles [4]. Furthermore, thinner needles cause less damage and reduce the chance of postdural puncture headache (PDPH) appearing after spinal anesthesia; indeed, the relative risk of PDPH decreases with reduction of needle diameter [5]. Moreover, flexible needles facilitate curved trajectories that can be desirable in order to avoid sensitive tissues, such as bone or blood vessels, which might lie between feasible entry points and potential targets. However, a major disadvantage to using thin flexible needles is that they are very difficult to control and do not lend themselves to intuitive (human) steering. Solving this problem of control requires development of a computerized robotic system that can plan and perform thin, flexible needle insertion. Creation of such a system represents a challenge for mechanical engineers and roboticists, but nevertheless is an urgent therapeutic goal since it will reduce morbidity and patient suffering after percutaneous procedures.

Devising a method to predict flexible needle motion was first addressed by DiMaio *et al.* [2]. A limitation of this work is that, due to the computation complexity, it does not allow for real-time simulation and control of the needle insertion. An active flexible steering system using shape memory alloys has been suggested for steering a catheter [6]. However, such a system is not suitable for thin needle navigation because of its size limitations. Several groups have focused on calculating the effects of needle bending. Kataoka *et al.* investigated needle deflection due to the bevel of the tip during linear needle insertion and expressed the deflection as a function of the driving force [7]. O'Leary *et al.* demonstrated experimentally that needle bending forces are significantly affected by the presence of a bevel tip [8]. Ebrahimi *et al.* have generated needle bending by incorporating a prebent stylus inside a straight canula [9]. This effect, intuitively used by clinicians, was modeled as a nonholonomic kinematics problem for steering of a highly flexible needle through a firm tissue [10]–[12]. It is notable that the effect of the beveled tip decreases with reduction of the needle diameter since the lateral force is proportional to the area of the tip.

Manuscript received October 4, 2006. This paper was recommended for publication by Associate Editor J. Troccaz and Editor F. Park upon evaluation of the reviewers' comments.

D. Glozman is with the Medical Robotics Laboratory, Technion—Israel Institute of Technology, Haifa, Israel, 32000 (e-mail: glozmand@technion.ac.il).

M. Shoham is with the Faculty of Mechanical Engineering, Technion—Israel Institute of Technology, Haifa, Israel, 32000 (e-mail: shoham@tx.technion.ac.il).

Color versions of one or more of the figures in this paper are available online at http://ieeexplore.ieee.org.

Digital Object Identifier 10.1109/TRO.2007.898972

1552-3098/$25.00 © 2007 IEEE

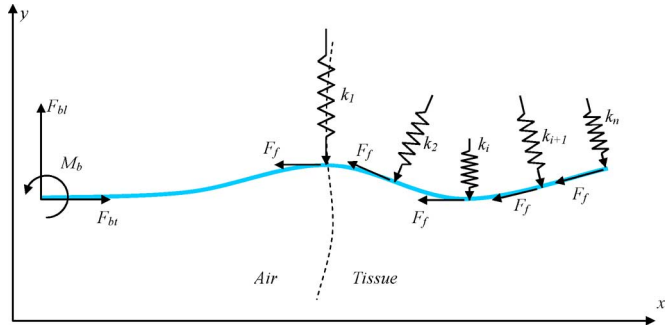

Fig. 1. Virtual springs model: the interaction of the tissue with the needle is modeled by distributed virtual springs.

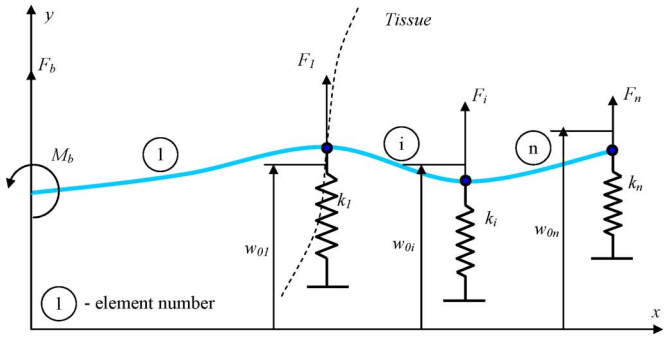

Fig. 2. Linear system model. Flexible beam subjected to a number of virtual springs.

It was demonstrated by the authors that the needle tip path is not unique and can be optimized to minimize lateral pressure of the needle body on the tissue [13]. The present investigation describes an algorithm that allows fast path planning and real-time tracking of a flexible needle insertion procedure. The aim of this investigation is the creation of an image-based closed-loop system for controlled flexible needle insertion that avoids obstacles.

II. System Configuration and Analytical Model

A. Virtual Springs Model

In this investigation, the modeling of flexible needle movements is based on the assumption of quasi-static motion; the needle is in an equilibrium state at each step. It is known that needle deflection due to interactions with biologic soft tissue is nonlinear with strain. However, the work of Simone *et al.* implies that it is reasonable to assume a linear lateral force response for small displacements [8], [14]. Thus, the tissue forces on the needle are modeled as a combination of lateral virtual springs distributed along the needle curve plus friction forces tangent to the needle. Since the tissue elastic modulus changes as a function of strain, the coefficients of the virtual springs are updated according to the strain-dependent dynamic elastic modulus and the system is linearized at each step. The concept is illustrated in Fig. 1.

As the shape of the needle changes, the location and orientation of the virtual springs change accordingly. The linearized system model yields the shape of the needle at each step. There is no physical meaning for the free length of the virtual springs. The only important parameter of a spring is the local stiffness coefficient that expresses the force of the tissue on the needle as a function of local displacement. The stiffness coefficients of the virtual springs are determined experimentally or by using preoperative images assuming empiric stiffness values of tissues and organs [16].

B. Linearized System Solution

Assuming small displacements, the needle is approximated by a linear beam subjected to point forces, as shown in Fig. 2. With appropriate spacing of elements, it can approximate a flexible beam according to the elastic foundation model.

At each joint, the force applied by a virtual spring is proportional to the displacement of the spring from its initial position

$$F_i = k_i(w_i - w_{0i}) \tag{1}$$

where k_i is the virtual spring coefficient, w_i is displacement at point i, and w_{0i} is the position of freed spring i.

Since the forces are a function of the deflection, the needle movement cannot be modeled by treating the beam as one element. Therefore, the beam is split into a number of elements, so that each beam element is subjected to two neighboring forces. Thus, the first element is the part of the needle outside of the tissue, and the remainder of the elements are distributed along the inner part according to the level of discretization. Each element behaves as a linear beam subjected to shearing forces at its borders. The displacement of each element is given by a third-degree polynomial. Using the nodal degrees of freedom from finite-elements theory, the coordinates are identified specifically with a single nodal point and represent a displacement or rotation, having clear physical interpretation. The displacement $y(x)$ has the form

$$y(x) = N_1\phi_1 + N_2\phi_2 + N_3\phi_3 + N_4\phi_4 \tag{2}$$

where N_1, N_3 are the coordinates and N_2, N_4 are the slopes at $x = 0$ and $x = l$ of an element, respectively. ϕ_i's are the shape functions of third degree.

The boundary conditions at the base are the position Y and the slope Θ of the first element

$$\begin{aligned} w_0(0) &= Y \\ \left.\frac{dw_0}{dx}\right|_{x=0} &= \theta. \end{aligned} \tag{3}$$

Second-order continuity between elements leads to

$$\begin{aligned} w_i|_{x=l} &= w_{i+1}|_{x=0} \\ \left.\frac{dw_i}{dx}\right|_{x=l} &= \left.\frac{dw_{i+1}}{dx}\right|_{x=0} \\ \left.\frac{d^2w_i}{dx^2}\right|_{x=l} &= \left.\frac{d^2w_{i+1}}{dx^2}\right|_{x=0}. \end{aligned} \tag{4}$$

Bending moment at the last element is negligible, hence

$$M_n|_{x=l} = \left.\frac{d^2w_n}{dx^2}\right|_{x=l} = 0. \tag{5}$$

Virtual spring forces are applied between each two successive elements, with magnitude of the product of the local spring stiffness coefficient and the displacement of the node from the initial penetration position

$$V_i = EI \left.\frac{d^3 w_i}{dx^3}\right|_{x=l} = \sum_{j=i}^{n} k_j (w_i|_{x=l} - w_{0,i}). \tag{6}$$

Finally, we have $4 \times n$ equations, where n is a number of elements.

$$\boldsymbol{KN} = \boldsymbol{Q} \tag{7}$$

where $\boldsymbol{K}$ is the matrix of coefficients of $N_{i,j}$ translation and slope degrees of freedom, $\boldsymbol{N}$ is the vector of $N_{i,j}$, where i is the element number and j is the degree of freedom of element i, and $\boldsymbol{Q}$ is a combination of stiffness coefficients and initial positions of the nodes at the times of their penetration with the needle $w_{0,i}$.

C. Forward and Inverse Kinematics

Given the translation and a rotation of the needle base, (7) is used to calculate the three-degree-of-freedom (3-DOF) translation and rotation of the needle tip, which is the forward kinematics solution.

In an actual needle insertion problem, there is a need to hit the target with the tip while at the same time avoid possible organ obstacles. Thus, a particular trajectory is desired for the tip of the needle, and it is the manipulation done at the needle base that is calculated. This is an inverse kinematics problem; namely, given the position and orientation of the tip trajectory, the translation and orientation of the needle base are derived.

Let us expand the matrix (7) as

$$\left[\begin{array}{ccc|cc} 1 & 0 & \cdots & 0 & 0 \\ 0 & -1 & \cdots & 0 & 0 \\ \hline & & & & \\ & K_{21} & & K_{22} & \end{array}\right] \begin{pmatrix} N_{11} \\ N_{12} \\ \vdots \\ N_{n3} \\ N_{n4} \end{pmatrix} = \begin{pmatrix} Y \\ \theta \\ \vdots \\ \vdots \\ \vdots \end{pmatrix}. \tag{8}$$

Given the base displacement Y and slope θ, one can solve for $N_{i,j}$. Note that the last two elements of vector $\boldsymbol{N}$ are the displacement and slope of the tip. In the inverse kinematics problem, the displacement and slope of the tip N_{n3}, N_{n4} are known and the unknowns are the displacement and slope of the base Y and θ or N_{11} and N_{12}. Since in the last two equations the two variables are known, we can write (8) as

$$\begin{aligned} [K_{21}]\tilde{N} &= \tilde{Q} - K_{22}\begin{pmatrix} N_{n3} \\ N_{n4} \end{pmatrix} \\ Y &= N_{11} \\ \theta &= N_{12} \end{aligned} \tag{9}$$

where $\tilde{\boldsymbol{N}}, \tilde{\boldsymbol{Q}}$ are the original vectors $\boldsymbol{N}, \boldsymbol{Q}$ without the last two elements. $\boldsymbol{K}_{21}$ is $(\mathrm{n}-2) \times (\mathrm{n}-2)$ matrix and (9) can be solved for $\tilde{\boldsymbol{N}}$ and therefore for Y and θ, which is the solution of the inverse kinematics.

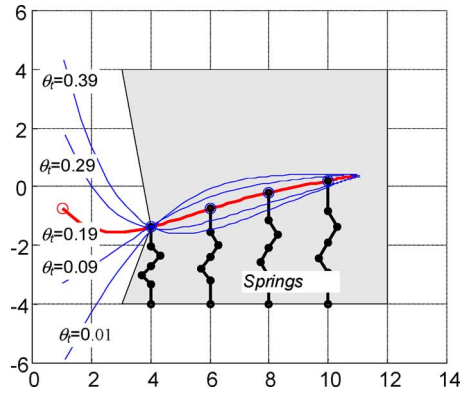

Fig. 3. Different needle path solutions for the same tip position with different tip inclinations.

D. Path Planning and Optimization

Planning a linear insertion path is trivial. The main challenge is avoiding obstacles while applying minimal lateral pressure on the tissue. In the presence of obstacles, the optimal needle path is one where there is minimal curvature of the needle. The path-planning problem thus reduces to finding the shortest curve that connects the target to the needle insertion point, which avoids the obstacle while maintaining minimal needle curvature.

Since every step is dependent on the history of the insertion, full simulation of the needle insertion is required. Fig. 3 shows several solutions of the path planning where the target point is reached with different tip inclinations.

Since, in biopsy, orientation of the tip is of less importance, one can choose from the infinite solutions the one that applies minimal pressure on the tissue. This is achieved by minimizing the sum of squares of the virtual springs displacements w_i and slopes Θ_i, the sum of which is given by S with weighting factors g_i to compensate for different units

$$S = \min \sum_{i=1}^{n} \left(w_i^2 + g_i \theta_i^2\right) = \min \sum_{i=1}^{n} \sum_{j=1}^{4} N_{ij}^2. \tag{10}$$

Differentiating (10) with respect to the desired tip orientation θ_t and equating to zero, we obtain

$$\frac{dS}{d\theta_t} = \sum_{i=1}^{n} \sum_{j=1}^{4} 2 N_{ij} \frac{dN_{ij}}{d\theta_t} = 0. \tag{11}$$

Equation (11) is then substituted into (8) in place of the equation of the slope of the last element N_{4n}, and the solution of (11) gives the optimized needle shape.

III. Controlled Flexible Needle Insertion

The control algorithm for determining the needle trajectory is shown in Fig. 4. The input to the system r_{nd} is the desired location of the needle tip excluding its orientation, which is later optimized by the controller (index d is for DESIRED and n is the iteration number). The controller is an inverse kinematics solution of the flexible needle, as described earlier, plus optimization for minimal needle deflections. The controller input is the desired position of the needle tip r_{nd} plus the error e_{n-1} from previous iterations. The controller output is the required coordinates of

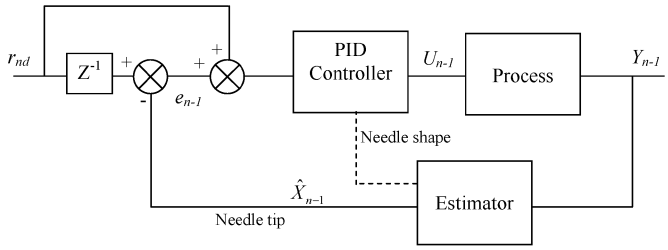

Fig. 4. Control loop diagram.

the needle base U_{n-1}. The dashed line from the estimator to the controller transfers the current needle shape from which springs stiffness coefficients are updated. The process outputs are the coordinates of the needle tip that are estimated by the image processing.

A. Needle Detection

1) Image Distortion Correction: Images acquired using standard X-ray equipment suffer typically from two independent geometric distortions: the geometry of the intensifier generates a pincushion distortion and the interaction of the Earth's magnetic field generates an imager-orientation dependent S-shaped distortion. Images of a calibration grid fixed to the image intensifier are used for detection and subsequent compensation for these distortions; this is known as the dewarping procedure [17]. The distortion is modeled by two bipolynomials, which model independently the distorted x_d and y_d calibration bead coordinates as a function of the undistorted calibration bead coordinates x_u and y_u as

$$x_d = \sum_{i=0}^{N}\sum_{j=0}^{M} P_{i,j}(x_u)^i(y_u)^j$$
$$y_d = \sum_{i=0}^{N}\sum_{j=0}^{M} Q_{i,j}(x_u)^i(y_u)^j \qquad (12)$$

where $P_{i,j}$ and $Q_{i,j}$ are the coefficients of the degree N, M of bipolynomials. Using the matched distorted and undistorted bead positions, a system of linear equations is constructed and solved by QR factorization to recover the coefficients $P_{i,j}$ and $Q_{i,j}$. We used fourth-degree bipolynomials which correct most of the fluoroscopic image distortions [17].

2) Needle Detection: A typical needle image is shown in Fig. 5(a). Detection begins from the needle base and follows the needle body from that point. The flexible (spinal) needle has a clearly detectable base shape, and its location is detected by normalized cross correlation of the original image with the filter shown in Fig. 5(c). Cross correlation is a very efficient tool to match images. It is quite robust to noise and can be normalized to allow pattern matching independently of scale and offset in the images [18].

Cross correlation with the whole image is performed only once. Following the first detection the filter is cross correlated with only a small square around the previously detected coordinates to save execution time and to avoid false detections. The rest of the needle is tracked by following the low gradient area of the 3-D representation of the image as shown in Fig. 6.

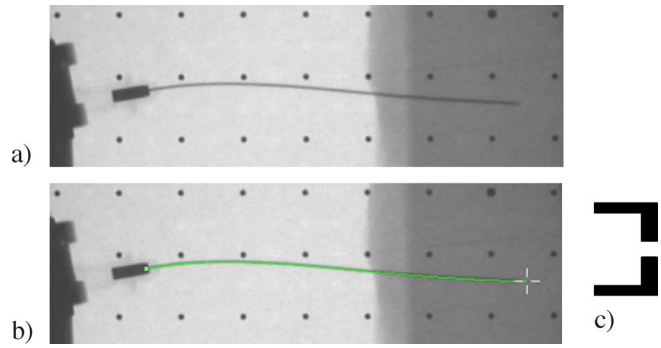

Fig. 5. Needle detection on the X-ray image.

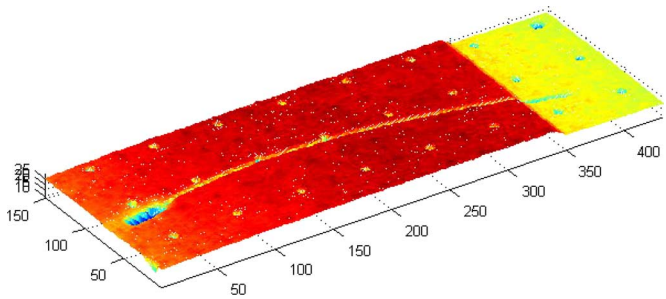

Fig. 6. 3-D needle image representation.

Needle tip detection is not straightforward. The surrounding soft tissue is not totally X-ray radiolucent, and the difference in gray shades between the tissue and the needle is small. Also, any obstruction, like beads, can make needle tip detection very difficult. Since the length of the needle is constant, it represents an additional parameter useful for determining the position of the needle tip. Therefore, in addition to gray-shade differences, the length of the needle is accounted for at each step.

Because of the noisiness of images, not all of the detected points lie on the real needle projection, therefore the needle is fitted using a seventh-degree polynomial that smoothes the noisy data. The detected needle shape is shown in Fig. 5(b).

B. Tracking Error and Control Definition

The control error is defined as the positional deviation of the tip from the planned trajectory. The error is calculated at each step, and the next requested needle position is set into the planned curve direction with magnitude determined by the PID controller.

C. Detection of Tissue Stiffness Properties From the Needle Shape

Since a vision system is utilized in detecting the shape of the needle, it is possible to obtain the properties of the tissue from the response of the needle, namely from the needle shape. During the insertion, the points where the virtual springs are penetrated and the position and orientation of the elements nodes are tracked.

In the construction of (8), the concentrated force boundary condition between the elements was used and is defined by

$$EI\frac{d^3V}{dx^3} = k_n(N_{n,3} - w_{0,n}) + k_{n+1}(N_{n+1,3} - w_{0,n+1}) \qquad (13)$$

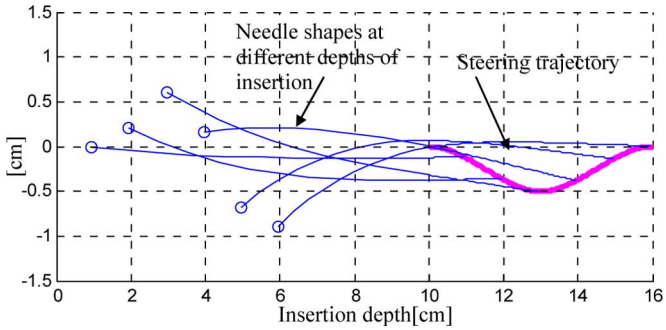

Fig. 7. Typical flexible needle steering.

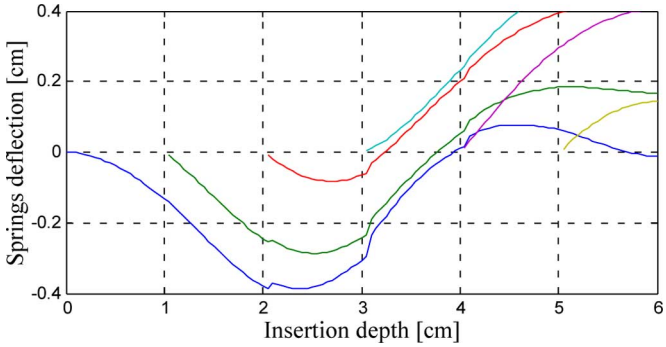

Fig. 8. Deflections of virtual springs from their relaxed length.

where the expression $(N_{n,3} - w_{0,n})$ represents the deflection of the spring $N_{n,3}$ from its relaxed position $w_{0,n}$ and for the last tip element is

$$EI\frac{d^3V}{dx^3} = k_n(N_{n,3} - w_{0,n}) \tag{14}$$

since the last element length is shorter than any other and the moment applied on it is negligible

$$\frac{d^3V}{dx^3} = \frac{12N_{n,1}}{l_n^3} - \frac{6N_{n,2}}{l_n^2} - \frac{12N_{n,3}}{l_n^3} - \frac{6N_{n,4}}{l_n^2}. \tag{15}$$

When the shape of the needle is known, the values of displacements and slopes at the nodes are calculated as well as the moments at the nodes using finite-difference approximation of d^3V/dx^3 [see (15)]. Then, starting from the last node, the stiffness coefficients of the springs are calculated from (13) as

$$k_n = \left[EI\frac{d^3V}{dx^3} - k_{n+1}(N_{n+1,3} - w_{0,n+1})\right] / (N_{n,3} - w_{0,n}). \tag{16}$$

A typical flexible needle insertion is shown in Fig. 7, causing the needle tip to follow a half sine wave. The stiffness coefficients of the virtual springs are taken as 10 N/mm. Fig. 8 depicts the deflections of the six virtual springs along the trajectory; each spring engages only when the tip passes its location.

The stiffness coefficients of the springs are calculated from the spline fitted needle shape shown as a function of the tip depth (Fig. 9). When the displacement of a spring is very small, it is impossible to calculate accurately the stiffness of the spring from (9) because of division by a very small number. The graphs depicting calculated stiffness coefficients are shown only for values of deflection larger than 0.05 mm. It can be seen that the graphs converge to the simulated value of the spring coefficient, which is 10 N/mm. The stiffness coefficient value is considered to be reliable after three successive iterations (blue circle).

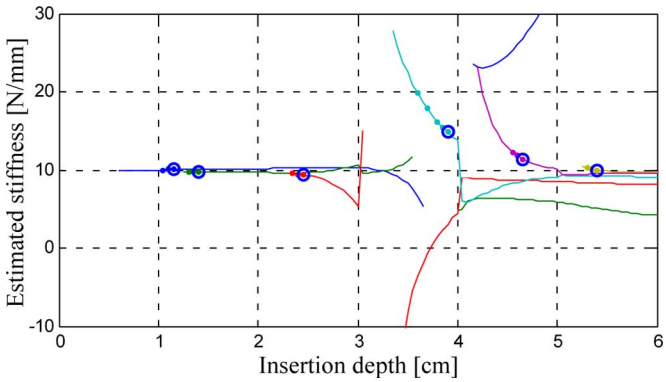

Fig. 9. Estimated stiffness coefficients of virtual springs.

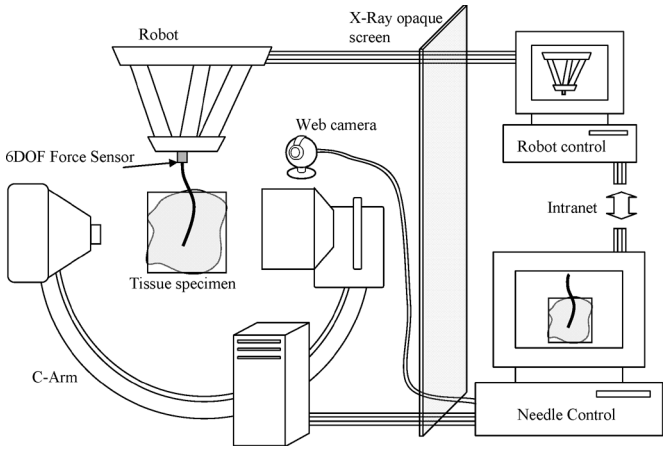

Fig. 10. Equipment used in controlled flexible needle insertion.

An advantage of this method is the ability to estimate or correct for tissue stiffness at the time of the insertion without any prior knowledge.

IV. Experimental System

A. Instrumentation

The experimental setup is shown in Fig. 10. The scene is divided into two sections separated by an X-ray opaque shield made of a lead sheet. The C-Arm is a Siemens Multimobil 5C with nominal intensifier diameter of 230 mm and highest image resolution of 756 × 562 pixels. The digital image was received from one of the C-Arm monitors by a DFG/1394-1e video-to-FireWire converter from Imaging Source Europe GmbH. In order to facilitate the experiment, a Logitech USB digital camera was placed facing the robot, and the needle and tissue sample were viewed on the user's screen.

Although the experiments were performed in 2-D space, we used a RSPR 6-DOF parallel robot shown in Fig. 11(a), designed previously for laparoscopic application [19]. The robot workspace can be approximated by a cylinder of 25-mm diameter and 50-mm height, which can be covered with plate angles of up to 20°. The needle is connected to a robot moving plate

Fig. 11. (a) RSPR 6-DOF parallel robot. (b) 6-DOF force sensor holding the needle.

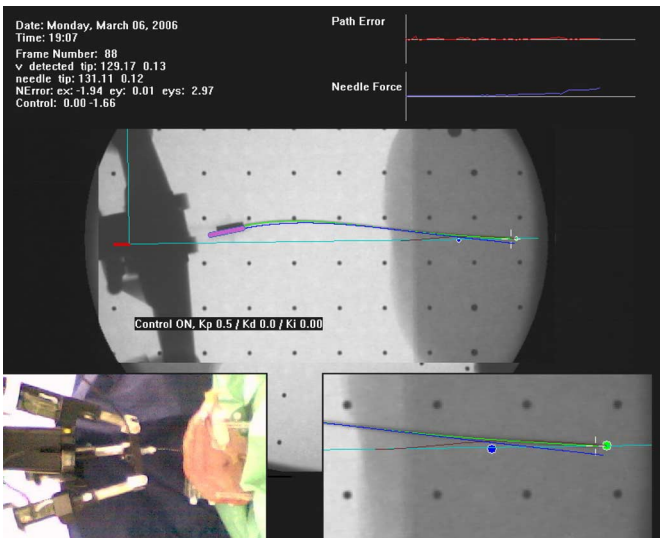

Fig. 12. Needle control computer screenshot.

by an ATI Nano17 6-DOF force/torque transducer, which measures needle insertion forces and torques.

A separate computer performs the calculations determining robot control and runs the robot control loop at 500 Hz. The main computer is the needle control computer that controls the motions of the robot via a local network. The control loop is responsible for sampling the network for incoming packets from the main computer, which can be movement orders, position, or force requests. The main computer has a Pentium IV 2.8-GHz processor and is responsible for the image processing, needle and tissue detections, as well as needle control. The main computer screen is shown in Fig. 12.

B. Needle Insertion Preparation

Several procedures must be completed in preparation for the insertion process; for example, an X-ray image distortion correction procedure, robot to image registration, tissue preparation, obstacles and target detection, and initial measurements of qualitative tissue properties.

1) Robot to Image Registration: Since the robot is not affixed to the C-Arm and each one has its own coordinate system, there is a need to register one to the other in orientation and scale. In order to accomplish this, the robot is requested to reach three known points in its workspace. From these points, the position, orientation, and scale of the robot coordinate system relative to the image coordinate system is established.

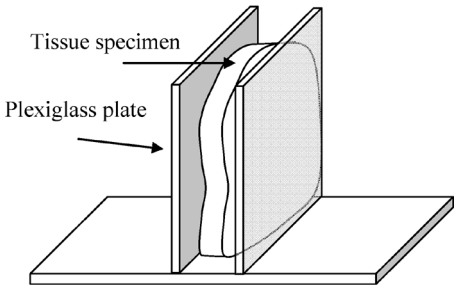

Fig. 13. Tissue specimen holder.

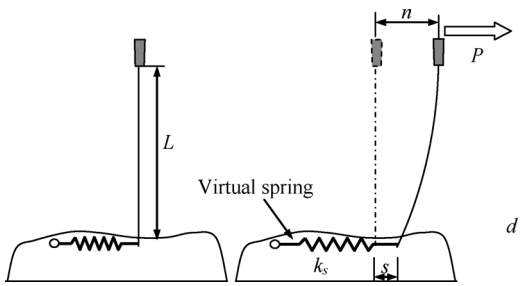

Fig. 14. Qualitative tissue stiffness measurement.

2) Tissue Preparation: We performed ten experiments on two types of tissue: a fresh turkey breast muscle and a beef liver. A slice of 20-mm thickness was prepared with no bones. The tissue specimen was placed between two plexiglass plates to keep it in place and in a vertical position to keep it from slipping. The tissue holder is shown in Fig. 13.

3) Obstacles and Target Detection/Specification: Two metal spheres of 3-mm diameter were inserted into the tissue: one as the target and the other as the obstacle. The user is required to delineate the target and the obstacle on the X-ray image. Then, the spheres are detected in the delineated region in the same way that the calibration beads are detected. Since the target and the obstacle can move during needle insertion, their detection is performed at every sampling.

4) Needle Properties and Qualitative Tissue Properties Measurements: For the experiments, stainless (316) steel 22-gauge spinal needles were used that have an outer diameter of 0.711 mm and an inside diameter of 0.394 mm, which exhibit 193-GPa Young modulus and moment of inertia

$$I = \frac{\pi}{64}\left(d_o^4 - d_i^4\right) = 11.361 * 10^{-3}\ \text{mm}^4. \qquad (17)$$

The initial tissue stiffness coefficient is estimated by measuring the force and the deflection of the needle tip while touching the tissue (see Fig. 14).

The equivalent stiffness coefficient of the needle in this case is calculated from $k_n = 3EI/L^3$, and the stiffness coefficient of the virtual spring is proportional to the ratio of the needle base to tip displacement $k_s/k_n = (n-s)/s$.

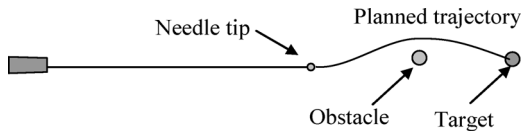

Fig. 15. Needle trajectory planning avoiding the obstacle.

C. Needle Insertion Procedure

Prior to needle insertion, the needle tip trajectory is examined to verify that the robot is capable of executing the required path and that the needle deflections are in the range of linear deflection approximation.

1) Needle Tip Trajectory Planning: A single fluoroscopic image is taken in order to plan the needle tip trajectory just before the insertion. The needle tip, the obstacle, and the target are detected on the image as described before, and through these three points a spline trajectory is passed with the following constraints.

1) The trajectory is tangent to the needle at the tip.
2) The trajectory passes above or below the obstacle at a specified distance.
3) The curvature of the spline at the target point is zero.

A typical trajectory planning is shown in Fig. 15.

Based on the required trajectory, inverse kinematics are calculated for each incremental movement.

2) Automatic Needle Insertion: After the trajectory has been verified for attainability and applied force, the software is ordered to start the execution. Since our low-power C-Arm (Siemens Multimobil 5C) blurs the image while the robot is in motion, we had to stop the robot to take the X-ray image statically. A typical execution cycle took about 50 s during which 60 X-ray shots were taken. In a common C-Arm, dynamic images can be acquired with sufficient quality which allows the process to be completed in several seconds.

The user is sitting behind a lead shield watching the needle insertion scene by a camera as shown in Fig. 10. In case of emergency, the user can stop the whole procedure and retract the needle with a click of a button.

D. Experimental Results

The qualitative tissue property measurement as described above led to 220-N/m stiffness for the first tissue spring approximation. During the insertion, the estimated stiffness coefficients were between 200-300 N/m which is similar to the stiffness coefficients in [8].

First, flexible needle insertion along the trajectory described above was performed with open-loop control. The tracking error of the tip from the preplanned trajectory is shown in Fig. 16. The force and torque as measured at the base of the needle are shown in Fig. 17.

Then, the needle was inserted along the same trajectory controlled by the PI controller as described above with $Kp = 0.5$ and $Ki = 0.001$. The tracking error of the tip from the preplanned trajectory is shown in Fig. 18. The force and torque as measured at the base of the needle are shown in Fig. 19.

The tracking error reaches 1.5 mm if no control is applied (Fig. 16), but with PID control the tracking error remains below 0.5 mm (Fig. 18). The force applied on the needle base is 25% greater during the controlled insertion while the moment is of the same magnitude (compare Figs. 17 and 19). It can be seen that the controlled flexible needle manipulation requires no significant additional forces and that the PID keeps successfully the tracking error within legitimate boundaries.

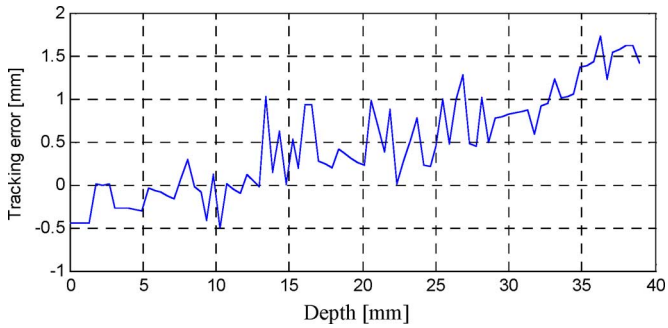

Fig. 16. Needle-tip tracking error during insertion with open-loop control.

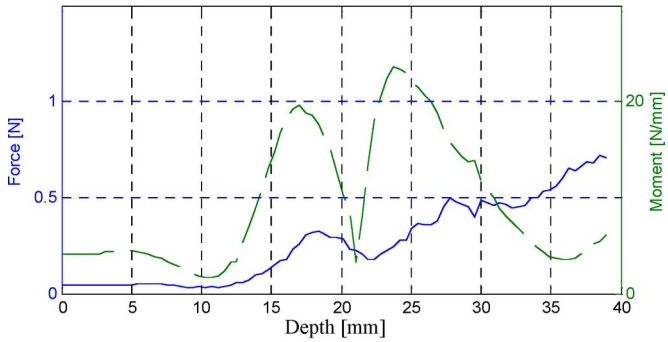

Fig. 17. Needle base force/torque sensor during insertion with open-loop control (force: solid line; moment: dashed line; absolute value).

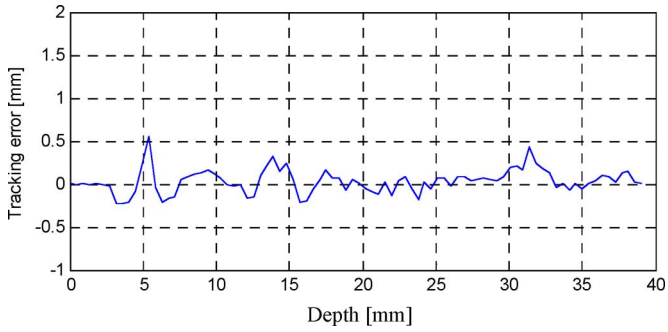

Fig. 18. Needle-tip tracking error during insertion with PI control.

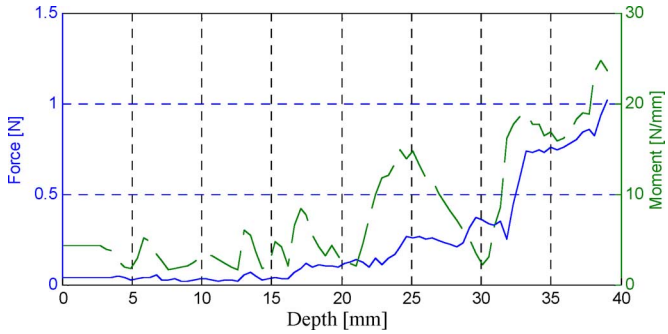

Fig. 19. Needle base force/torque sensor during insertion with PI control (force: solid line; moment: dashed line; absolute value).

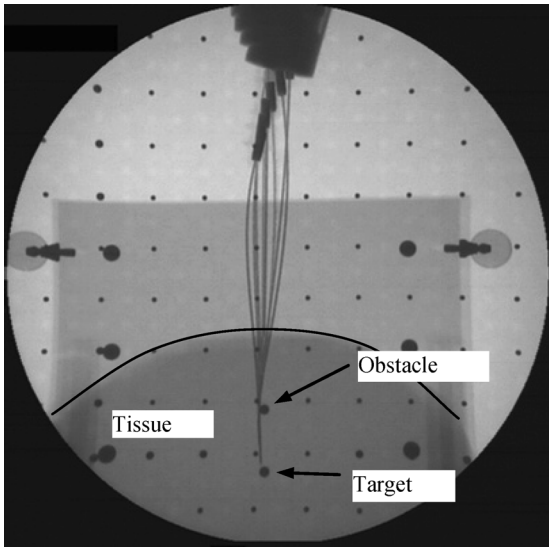

Fig. 20. Controlled needle insertion in a turkey breast tissue.

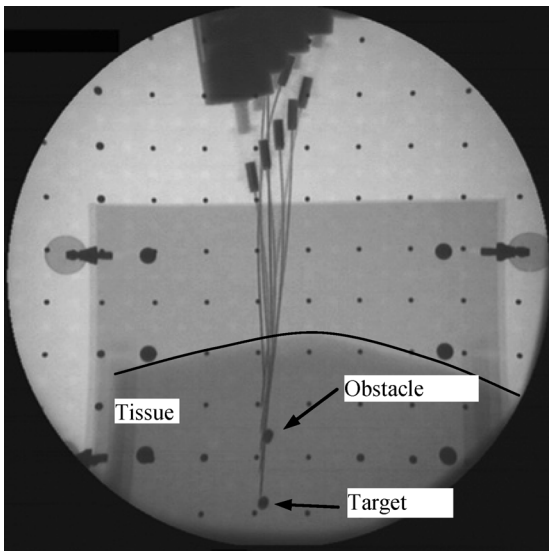

Fig. 21. Controlled needle insertion in a beef liver tissue.

The X-ray sequence of controlled flexible needle insertion into two different tissues and by two different trajectories are depicted in Figs. 20 and 21. Note that the obstacle and target points appear as oval since they move during the procedure.

V. Conclusion

This paper describes the development of a closed-loop control system for flexible needle steering with real-time X-ray imaging. The flexible needle–tissue interaction is modeled in 2-D by a system of virtual linear springs. Using this model, the inverse and forward kinematics of needle insertion are calculated in one step by solving a low-dimensional linear system of equations. The model enables path planning and its optimization for minimal tissue pressure. It is demonstrated here that this model can be solved in a closed form for a given needle tip trajectory. Relaxing the requirement that tip orientation be tangent to the path at each point decreases greatly both the needle base stroke and the lateral pressure exerted on the tissue.

The model was tested experimentally by a 6-DOF robot, which was used to maneuver the needle base and insert the needle into animal tissues, verifying the proposed concept. The system was given the starting needle, obstacles, and target locations, from which the optimal needle tip trajectory was calculated in terms of minimal pressure on the surrounding tissue. Along the 40-mm trajectory that avoids the obstacle and hits the target, the error stayed below the 0.5-mm level.

Future work will include applications of additional control schemes and expanding the model to 3-D. Experiments using faster X-ray systems would considerably reduce needle insertion time.

References

[1] J. De Andres, M. A. Reina, and A. Lopez-Garcia, "Risks of regional anesthesia: Role of equipment—Needle design, catheters," in *Proc. VII Annu. Eur. Soc. Regional Anaesthesia Congress*, Geneva, Switzerland, Sep. 16–19, 1998.

[2] S. P. DiMaio and S. E. Salcudean, "Needle steering and model-based trajectory planning," in *Proc. Medical Image Comput. Comput.-Assisted Intervention*, Montreal, QC, Canada, 2003, vol. LNCS 2878, pp. 33–40.

[3] R. Alterovitz, J. Pouliot, R. Taschereau, I. J. Hsu, and K. Goldberg, "Sensorless planning for medical needle insertion procedures," in *Proc. IEEE/RSJ Int. Conf. Intell. Robots Syst.*, Oct. 2003, pp. 3337–3343.

[4] A. Grant and J. Neuberger, "Guidelines on the use of liver biopsy in clinical practice," *Brit. Soc. Gastroenterol. Gut*, vol. 45, no. Suppl. 4, pp. IV1–IV11, 1999.

[5] U. Chohan and G. A. Hamdani, "Post dural puncture headache," *J. Pakistan Med. Assoc.*, vol. 53, no. 8, pp. 359–366, Aug. 2003.

[6] T. Mineta, T. Mitsui, Y. Watanabe, S. Kobayashi, Y. Haga, and M. Esashi, "Batch fabricated flat meandering shape memory alloy actuator for active catheter," *Sens. Actuators A: Phys.*, vol. 88, pp. 112–120, 2001.

[7] H. Kataoka, T. Washio, M. Audette, and K. Mizuhara, "A model for relations between needle deflection, force, and thickness on needle penetration," in *Proc. Med. Image Comput. Comput. Aided Intervention*, 2001, pp. 966–974.

[8] M. O'Leary, C. Simone, T. Washio, K. Yoshinaka, and A. Okamura, "Robotic needle insertion: Effects of friction and needle geometry," in *Proc. IEEE Int. Conf. Robot. Autom.*, 2003, pp. 1774–1780.

[9] R. Ebrahimi, S. Okzawa, R. Rohling, and S. Salcudean, "Hand-held steerable needle device," in *Proc. Med. Image Comput. Comput.-Assisted Intervention*, 2003, pp. 223–230.

[10] W. Park, J. S. Kim, Y. Z. Cowan, A. M. Okamura, and G. S. Chirikjian, "Diffusion-based motion planning for a nonholonomic flexible needle model," in *Proc. IEEE Int. Conf. Robot. Autom.*, Barcelona, Spain, Apr. 2005, pp. 4611–4616.

[11] R. Alterovitz and K. Goldberg, "Planning for steerable bevel-tip needle insertion through 2D soft tissue with obstacles," in *Proc. IEEE Int. Conf. Robot. Autom.*, Barcelona, Spain, Apr. 2005, pp. 1652–1657.

[12] R. J. Webster, III, J. S. Kim, N. J. Cowan, G. S. Chirikjian, and A. M. Okamura, "Nonholonomic modeling of needle steering," *Int. J. Robot. Res.*, vol. 25, no. 5–6, pp. 509–525, May–Jun. 2006.

[13] D. Glozman and M. Shoham, "Flexible needle steering and optimal trajectory planning for percutaneous therapies," in *Proc. Med. Image Comput. Comput.-Assisted Intervention*, 2004, pp. 137–144.

[14] C. Simone and A. Okamura, "Haptic modeling of needle insertion for robot-assisted percutaneous therapy," in *Proc. IEEE Int. Conf. Robot. Autom.*, 2002, pp. 2085–2091.

[15] M. O'Leary, C. Simone, T. Washio, K. Yoshinaka, and A. Okamura, "Robotic needle insertion: Effects of friction and needle geometry," in *Proc. IEEE Int. Conf. Robot. Autom.*, 2003, pp. 1774–1780.

[16] Y. C. Fung, *Biomechanics: Mechanics Properties of Living Tissues*, 2nd ed. New York: Springer-Verlag, 1993, p. 277.

[17] G. Wolberg, *Digital Image Warping*. New York: Wiley-IEEE Computer Soc. Press, 1990.

[18] R. C. Gonzalez and R. E. Woods, *Digital Image Processing*. Upper Saddle River, NJ: Prentice-Hall, 2002.

[19] N. Simaan, D. Glozman, and M. Shoham, "Design considerations of new six degrees-of-freedom parallel robots," in *Proc. IEEE Int. Conf. Robot. Autom.*, 1998, vol. 2, pp. 1327–1333.

Daniel Glozman received the B.Sc. and M.Sc. degrees in mechanical engineering from the Technion—Israel Institute of Technology, Haifa, Israel, in 1998 and 2000, respectively, where he is currently working toward the Ph.D. degree. His M.Sc. thesis dealt with registration of 3-D objects for robot-assisted surgery.

His research interests are in the area of medical robotics, medical imaging, and medical devices. He was a Software Development Manager with Simpod Inc. from 2001 to 2003. He is currently with the Alfred Mann Institute for Biomedical Development at the Technion.

Mr. Glozman was the recipient of the Wolf Prize for outstanding Master's research in 1999.

Moshe Shoham (A'89) has been conducting research in robotic field for the past 15 years, with a special focus on kinematics and dynamics of robots, sensor integration, multifinger hands, and medical applications. He has been heading the Robotics Laboratories of the Mechanical Engineering Department, Columbia University, New York, and of the Technion-Israel Institute of Technology, Haifa, Israel. In 2001 he founded Mazor Surgical Technologies—a company that developed miniature surgical robots.

Prof. Shoham developed and constructed novel robotic systems for which he received several awards, including the Haifa City Award for Science and Technology, the Mitchell Entrepreneurial Award, the Hershel Rich Innovation Award, the Jolodan Prize, and the Kaplan Prize for innovative management in high technology. His research activity has been funded by grants from commercial companies as well as governmental agencies in Israel, the U.S., France, and Italy. From 2000 to 2002, he served as a Technical Editor for the IEEE TRANSACTIONS ON ROBOTICS AND AUTOMATION.